

1 Ice nucleation proteins self-assemble into large fibres to trigger 2 freezing at near 0 °C 3

4 Thomas Hansen¹, Jocelyn C. Lee¹, Naama Reicher², Gil Ovadia³, Shuaiqi Guo⁴, Wangbiao Guo⁴,
5 Jun Liu⁴, Ido Braslavsky³, Yinon Rudich², Peter L. Davies^{1*}
6

7 ¹Department of Biomedical and Molecular Sciences, Queen's University, Kingston, ON Canada
8 K7L 3N6

9 ²Department of Earth and Planetary Sciences, The Weizmann Institute of Science, Rehovot
10 7610001, Israel

11 ³The Robert H. Smith Faculty of Agriculture, Food and Environment, Institute of Biochemistry,
12 Food Science, and Nutrition, The Hebrew University of Jerusalem, Rehovot 7610001, Israel

13 ⁴Department of Microbial Pathogenesis, Yale University School of Medicine, New Haven, CT
14 06536

15 *Corresponding author: Peter L. Davies, peter.davies@queensu.ca
16

17 Abstract

18 In nature, frost can form at a few degrees below zero Celsius. However, this process requires the
19 assembly of tens of thousands of ice-like water molecules that align together to initiate freezing
20 at these relatively high temperatures. Water ordering on this scale is mediated by the ice
21 nucleation proteins of common environmental bacteria like *Pseudomonas syringae* and *P.*
22 *borealis*. However, individually, these 100-kDa proteins are too small to organize enough water
23 molecules for frost formation, and it is not known how giant, megadalton-sized multimers, which
24 are crucial for ice nucleation at high sub-zero temperatures, form. The ability of multimers to
25 self-assemble was suggested when the transfer of an ice nucleation protein gene into *E. coli* led
26 to efficient ice nucleation. Here we demonstrate that a positively-charged sub-domain at the C-
27 terminal end of the central beta-solenoid of the ice nucleation protein is crucial for
28 multimerization. Truncation, relocation, or change of the charge of this subdomain caused a
29 catastrophic loss of ice nucleation ability. Cryo-electron tomography of the recombinant *E. coli*
30 showed that the ice nucleation protein multimers form fibres that are ~ 5 nm across and up to 200
31 nm long. A model of these fibres as an overlapping series of antiparallel dimers can account for

32 all their known properties and suggests a route to making cell-free ice nucleators for
33 biotechnological applications.

34

35 **Introduction**

36 Ice crystals grow from ice embryos, which are crystalline aggregates of water molecules that
37 spontaneously form (homogeneous nucleation) in pure H₂O at approximately -38 °C (1). Ice can
38 arise in nature at much warmer temperatures because various surfaces act as stabilizers of ice
39 embryos (heterogeneous nucleation). Only once an ice embryo reaches a critical number of
40 organized water molecules will it become stable enough to spontaneously grow at elevated
41 temperatures, a process called ice nucleation (2). The most active heterogeneous ice nucleators
42 are bacterial ice nucleation proteins (INPs), which can stabilize an ice embryo at temperatures as
43 warm as -2 °C (3).

44

45 INPs are large proteins (up to ~150 kDa) that are thought to form multimers on the surface of the
46 bacteria that express them (4, 5). AlphaFold predictions have provided some insight into the INP
47 monomer structure (**Fig. 1A**). For the INP from *Pseudomonas borealis* (*PbINP*) AlphaFold
48 predicted a folded domain of ~100 residues at the N terminus followed by a flexible linker of
49 ~50 residues, a repetitive domain composed of 65 16-residue tandem repeats, and a small 41-
50 residue C-terminal capping structure (6). The predicted fold of the repetitive domain agrees with
51 some previous homology-based models in which each 16-residue repeat forms a single coil of a
52 β-solenoid structure (7, 8).

53

54 Most coils of the β-solenoid contain putative water-organizing motifs like Thr-Xaa-Thr (TXT)
55 that occupy the same position in each coil to form long parallel arrays, and where Xaa is an
56 inward pointing amino acid residue (**Fig. 1B**). Shorter versions of similar arrays have
57 convergently evolved in insects to form the ice-binding sites of several hyperactive antifreeze
58 proteins (AFPs) (9-11). According to the anchored clathrate water hypothesis, the ability of these
59 arrays to position ice-like water molecules facilitates AFP adsorption to the ice crystal surface
60 (12). In the ~10 times longer INPs, which additionally form multimers, the organizing effect on
61 nearby water molecules is thought to increase to the point where ice embryos can be stabilized
62 enough to lead to the spontaneous growth of ice at high sub-zero temperatures. Recently, we

63 demonstrated that interruptions in the continuity of these water-organizing motifs decrease the
64 ice nucleation temperature as much as extensive deletions of the water-organizing coils (6).

65
66 Previously we showed that the final 12 C-terminal coils lack the water organizing motifs and that
67 deleting these coils resulted in a near total loss of activity (6). Interestingly, the necessity for
68 these C-terminal coils was demonstrated by Green and Warren in 1986 in the first publication of
69 an INP sequence (13) but was not further investigated. While the water-organizing coils (WO-
70 coils) are characterized by their conserved TXT, SLT, and Y motifs, the defining feature of the
71 C-terminal-most coils, other than the lack of these motifs, is that position 12 of the 16-residue
72 coil is typically occupied by arginine. Thus, we refer to these non-WO-coils as R-coils. Since
73 both coil types maintain the same predicted fold but serve different functions, we consider them
74 subdomains of the same β -solenoid (14). In the WO-coils, position 12 is usually occupied by
75 residues of the opposite charge, Asp and Glu. This charge inversion is noteworthy as it has been
76 shown that electrostatic interactions contribute to the formation of INP multimers (15, 16). It has
77 also been shown that INP activity is affected by pH, which is consistent with a role for
78 electrostatic interactions (17). We and others have suggested that INPs may assemble through
79 salt-bridging of the sidechains in these positions of the coil (6, 18).

80
81 Multimerization of INPs was shown in 1988 by Govindarajan and Lindow, who used radiation
82 inactivation analysis to suggest a multimer size of 19 MDa (>100 monomers) (4). Computational
83 estimates indicate that up to a 5-MDa (34 INPs) structure of laterally assembled INPs is
84 necessary for optimal activity, which puts the multimer size in the same order of magnitude as
85 that determined experimentally (19). The tendency to form such large structures is one of many
86 factors that makes these proteins difficult to work with (3) and may be part of why, despite many
87 attempts, very little is known about them at a molecular level (20). The size of these structures
88 does, however, make them amenable to size-based separation from most proteins (21, 22). INP
89 multimers are also large enough to be visible using negative stain transmission electron
90 microscopy (TEM) on enriched samples, revealing a fibril-like morphology (22, 23).

91
92 In nature, these multimers form on the surface of bacteria, anchored to the outer membrane by
93 the N-terminal domain (24), which has been used extensively for the surface display of many

94 proteins (25, 26). When expressed recombinantly in *E. coli*, INPs have full activity suggesting
95 that multimers are able to form and that they are the product of self-assembly. Remarkably, INPs
96 with N-terminal truncations are only slightly less active, suggesting that assembly on the cell
97 surface is not mandatory, and it can occur in the cytoplasm whether anchored to the inner surface
98 of the plasma membrane or free in solution (27, 28).

99

100 Here, we have studied the role of the R-coils in INPs through a series of mutations and
101 rearrangements. Additionally, using cryo-focused-ion-beam (cryo-FIB) milling and cryo-electron
102 tomography (cryo-ET), we have observed the fibrillar morphology of INP multimers within cells
103 recombinantly expressing INPs. The R-coils' length, location, and sequence are critical for INP
104 multimerization and hence INP activity. Although we report results using *PbINP*, the
105 bioinformatic analysis presented here indicates that these findings are universally applicable to
106 the INP family, including the more commonly studied InaZ from *Pseudomonas syringae*.

107

108 **Results**

109 **Bioinformatic analysis reveals conservation in the number of R-coils across all INPs**

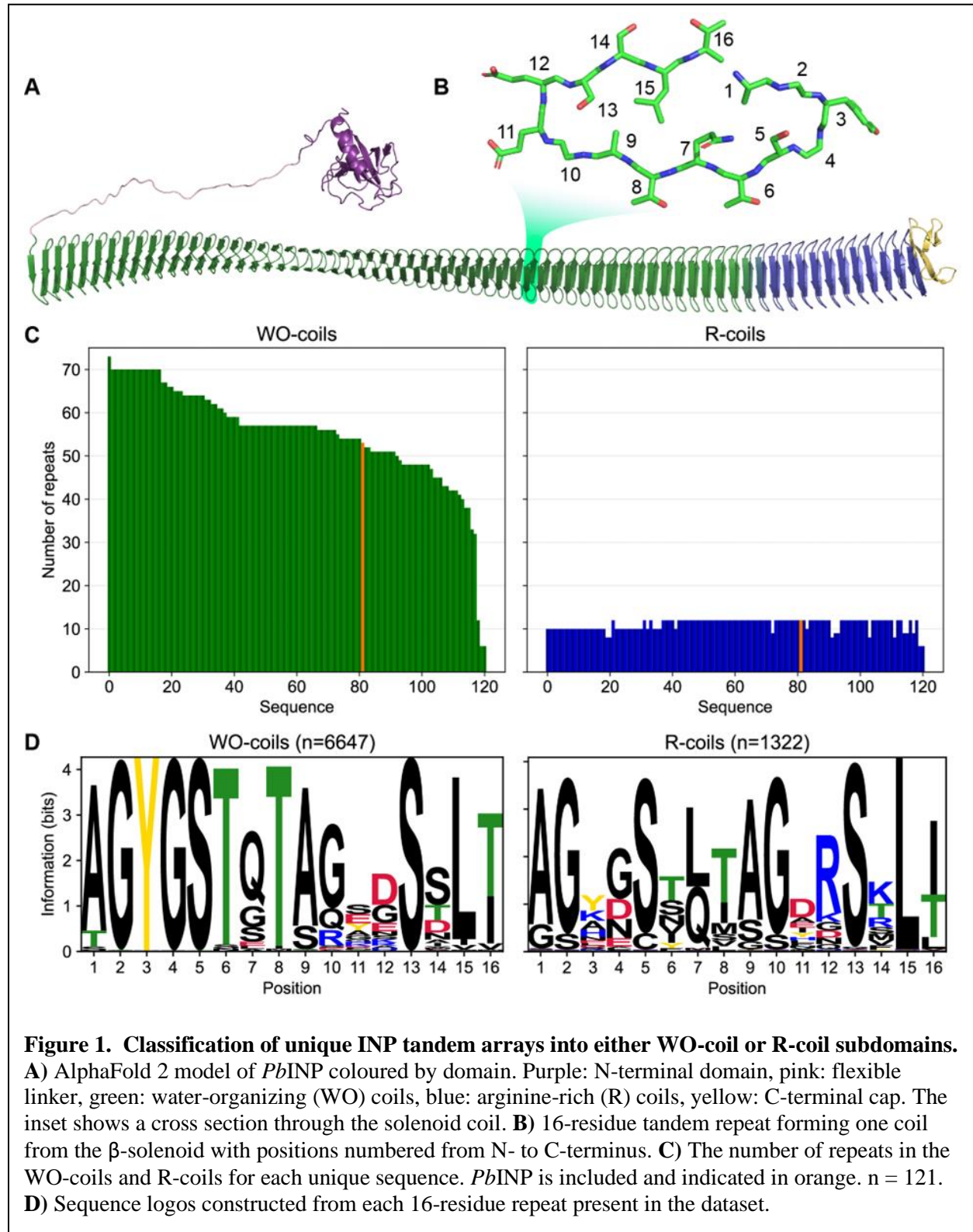
110 In *PbINP*, there are 53 WO-coils and 12 R-coils (**Fig. 1A**), each composed of 16 residues (**Fig.**
111 **1B**). To determine whether this ratio of coil types is consistent across known INPs, we analyzed
112 INP and INP-like solenoid sequences in the *nr* (NCBI) database. The long tandem arrays of coils
113 in INPs make them prone to mis-assembly when using short-read DNA sequencing (29) so we
114 opted to limit our dataset to sequences obtained by long-read technologies (Oxford Nanopore
115 and Pacific Biosciences SMRT sequencing). From this bioinformatics study, it is apparent that
116 the number of WO-coils varies considerably from over 70 coils to around 30, with a median
117 length of 58 coils (**Fig. 1C**). In contrast, the length of the R-coil region is much less variable
118 across sequences, with 107 of 120 sequences containing either 10 or 12 R-coils (**Fig. 1C**). The
119 stark difference in length variation between the numbers of WO-coils and the R-coils supports
120 the hypothesis that these two regions have different functions.

121

122 The differences observed between the *PbINP* WO-coil consensus sequence and the R-coil
123 consensus sequence, which include the loss of putative WO motifs in the former and the
124 appearance of basic residues at position 12 in the latter, are consistent across the entire dataset

125 **(Fig. 1D)**. This is apparent from the sequence logos comparing them. Also worth noting is the
126 similarity of the sequence logos for WO-coils and R-coils in *PbINP* (6) with those based on 120
127 sequences from the database.

128



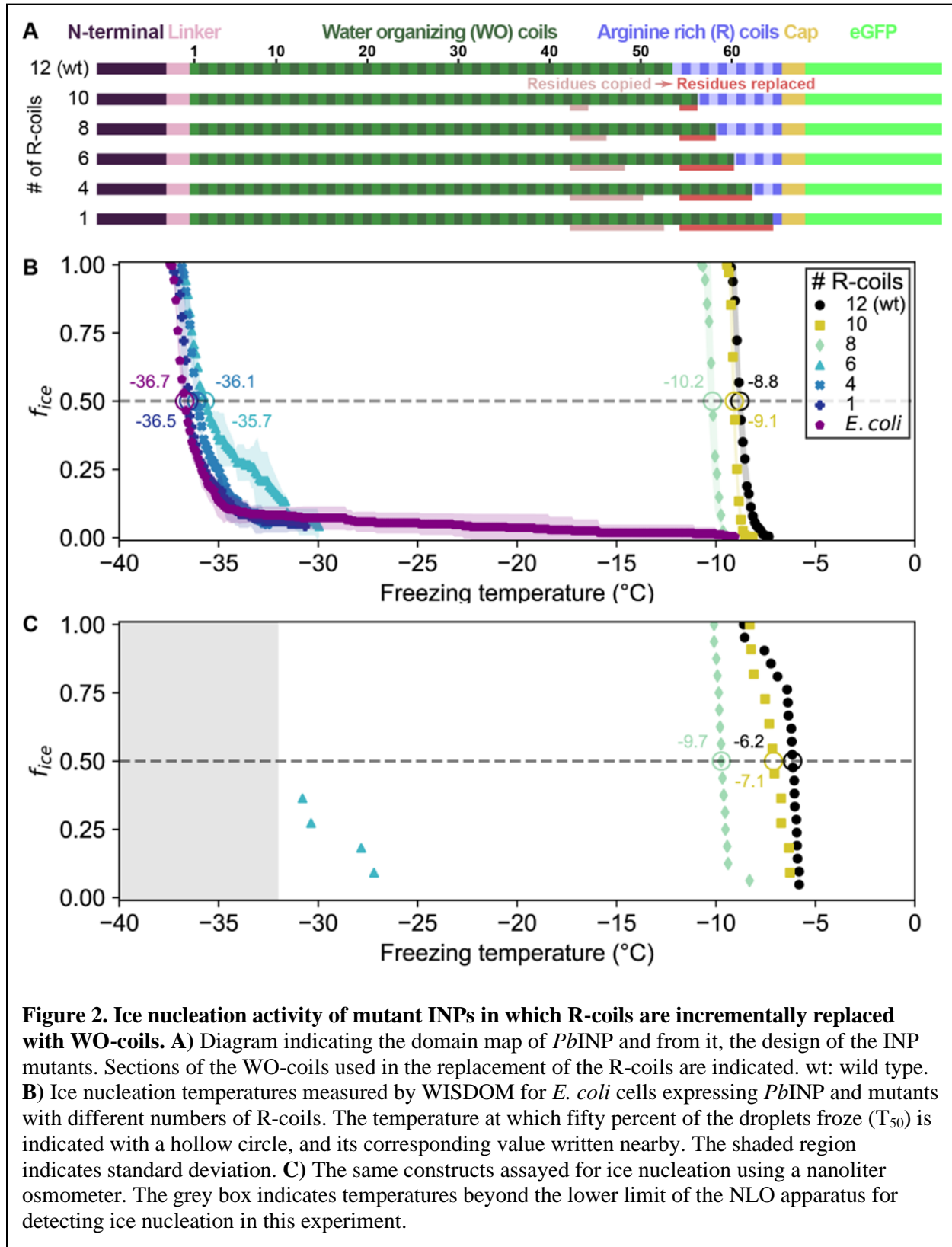
129

130

131 **Incremental replacement of R-coils with WO-coils severely diminishes ice nucleating**
132 **activity**

133 Given the remarkable conservation of the R-coil count compared to the variability of the WO-
134 coil numbers, we measured the functional impact of shortening the R-coil region. We designed
135 mutants in which the R-coils were incrementally replaced with WO-coils, shortening the R-coil
136 subdomain from 12 to 10, 8, 6, 4, or 1 coil(s), while retaining the same overall length as wild-
137 type *PbINP* (**Fig. 2A**). To avoid disrupting any potential interaction between the C-terminal cap
138 structure and the R-coils, one R-coil was left in place to produce the 1 R-coil mutant.

139
140 Ice nucleation assays were performed to assess the activity of the incremental replacement
141 mutants. In theory, replacement of R-coils by WO-coils could result in a gain of function as the
142 water-organizing surface increased in area. However, as the number of R-coils was reduced, the
143 nucleation temperature decreased (**Fig. 2B**). Replacing two or four R-coils to leave ten or eight
144 in place resulted in a slight loss of activity compared to the wild-type protein ($T_{50} = -9.1$ °C and -
145 10.2 °C, respectively, where T_{50} is the temperature at which 50% of droplets have frozen).
146 Reducing the R-coil count to six dramatically decreased the activity ($T_{50} = -35.7$ °C). The
147 construct with only four R-coils in place showed only the slightest amount of activity, and
148 activity was entirely lost in the construct containing only one R-coil. Evidently, small decreases
149 in the R-coil region length produce disproportionately large decreases in activity. Halving the
150 length of the R-coils by replacing just six coils reduced ice nucleation activity by 26.9 °C,
151 whereas reducing the WO-coil length in half decreased the T_{50} by less than 2 °C (6). Since the R-
152 coils mostly lack the motifs required for water-organizing, we attribute the observed changes in
153 nucleation temperature to changes in INP multimer formation.



156 **The location of the R-coil subdomain is crucial**

157 In addition to its length, we investigated whether the location of the R-coil subdomain is
158 important for ice nucleation activity. We produced constructs where 11 of the 12 R-coils were
159 relocated to either the N-terminal end of the solenoid or the approximate midpoint of the
160 solenoid (**Fig. 3A**). As before, the C-terminal R-coil was left in place adjacent to the cap
161 structure. We also produced an R-coil deletion construct, where the same 11 R-coils were deleted
162 entirely from the protein.

163

164 The N-terminal relocation construct displayed markedly lower activity with a $T_{50} = -22.4$ °C
165 compared to wild-type *PbINP*, and the midpoint relocation construct displayed almost no activity
166 ($T_{50} = -36.1$ °C), and was indistinguishable in activity from the construct where the R-coils were
167 deleted (**Fig. 3B**).

168

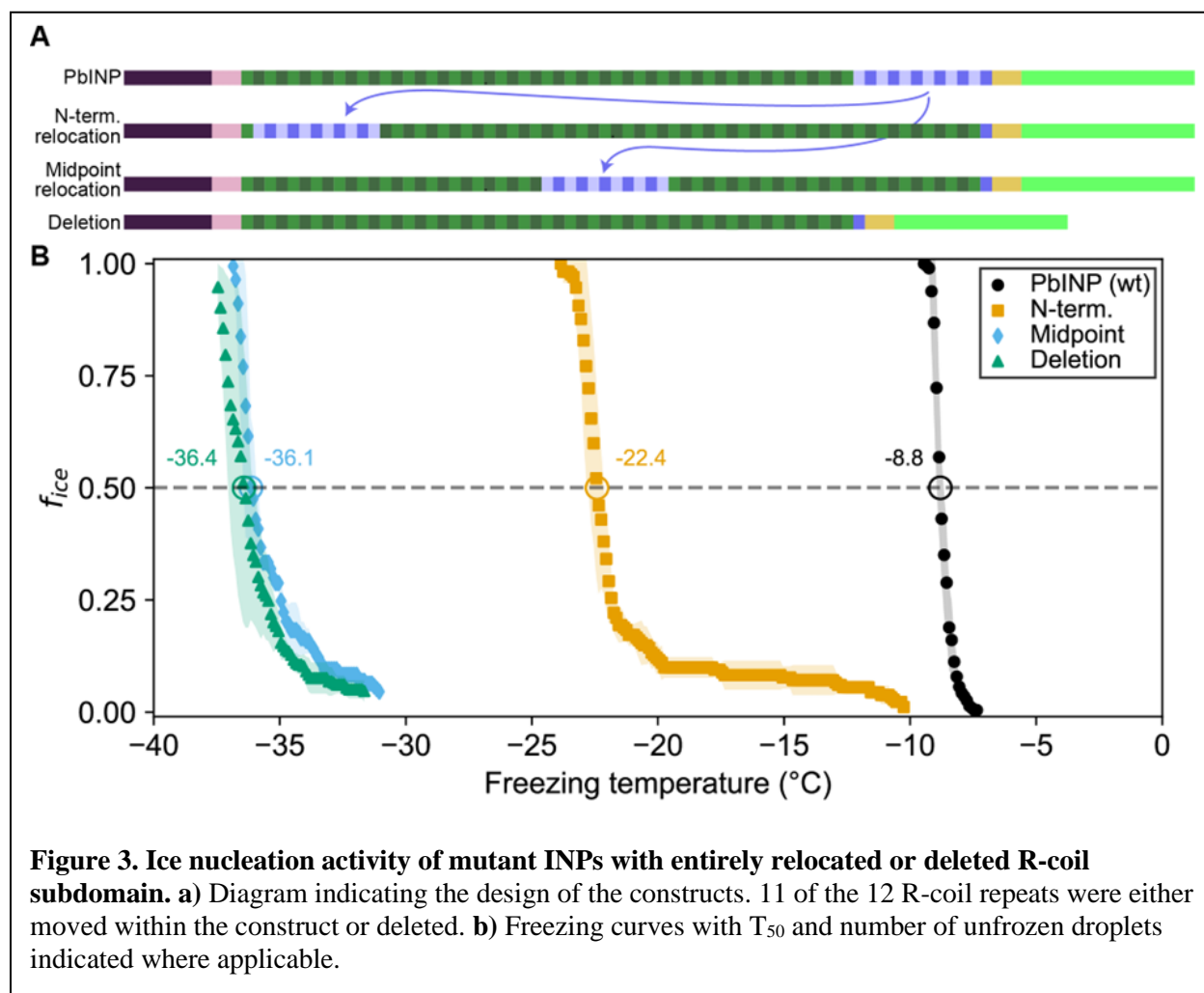


Figure 3. Ice nucleation activity of mutant INPs with entirely relocated or deleted R-coil subdomain. a) Diagram indicating the design of the constructs. 11 of the 12 R-coil repeats were either moved within the construct or deleted. b) Freezing curves with T_{50} and number of unfrozen droplets indicated where applicable.

169

170

171 Targeted mutations reveal that positively charged residues are important for R-coil 172 function

173 Having established the importance of R-coil position and length for high activity, we next
174 investigated the features of this subdomain that are required for its activity. Looking at the
175 charge distribution along the solenoid from N terminus to C terminus (**Fig. 4A**), we noted a
176 switch at the start of the R-coils from an abundance of acidic residues to their replacement by
177 basic residues. To probe the significance of this observation, we mutated all basic residues
178 (R/K/H) in the R-coils to match those found in the same repeat positions of the WO-coils (D/G/E
179 for positions 11 and 12, and S for position 14). In total, 17 basic residues – 10 Arginine (R), 4
180 Lysine (K), 3 Histidine (H) – were replaced in the R-coils to generate the RKH replacement
181 mutant. The side chains at these positions are predicted by the AlphaFold model to point outward

182 from the solenoid, so these mutations are unlikely to compromise the stability of the solenoid
183 core.

184

185 There was a 10.3 °C drop in T_{50} from wild-type activity after RKH replacement (**Fig. 4B**) ($T_{50} =$
186 -19.1 °C). Although this is a large decrease in activity, it was not as deleterious as the relocation
187 or deletion mutations (**Fig. 3**). The prominent, entirely conserved tyrosine in position 3 of the
188 WO-coils is only present in the first three R-coils and is missing from the following nine coils,
189 making it another candidate for mutation. Upon extending this “tyrosine ladder” through the R-
190 coils (**Fig. 4A**), there was a 1.3-°C loss in activity. However, when combining the RKH
191 replacement with the tyrosine ladder extension, an almost total loss of activity was observed (T_{50}
192 $= -36.1$ °C on WISDOM) (**Fig. 4B**).

193

194 In the final mutated *PbINP* construct in this series, all arginines in the R-coils were replaced by
195 lysines (K-coils). This mutant nucleated ice formation at essentially the same temperature as the
196 wild type (**Fig. 4b**) ($p = 0.89$), suggesting that positive charges in these locations are more
197 important than side chain geometry.

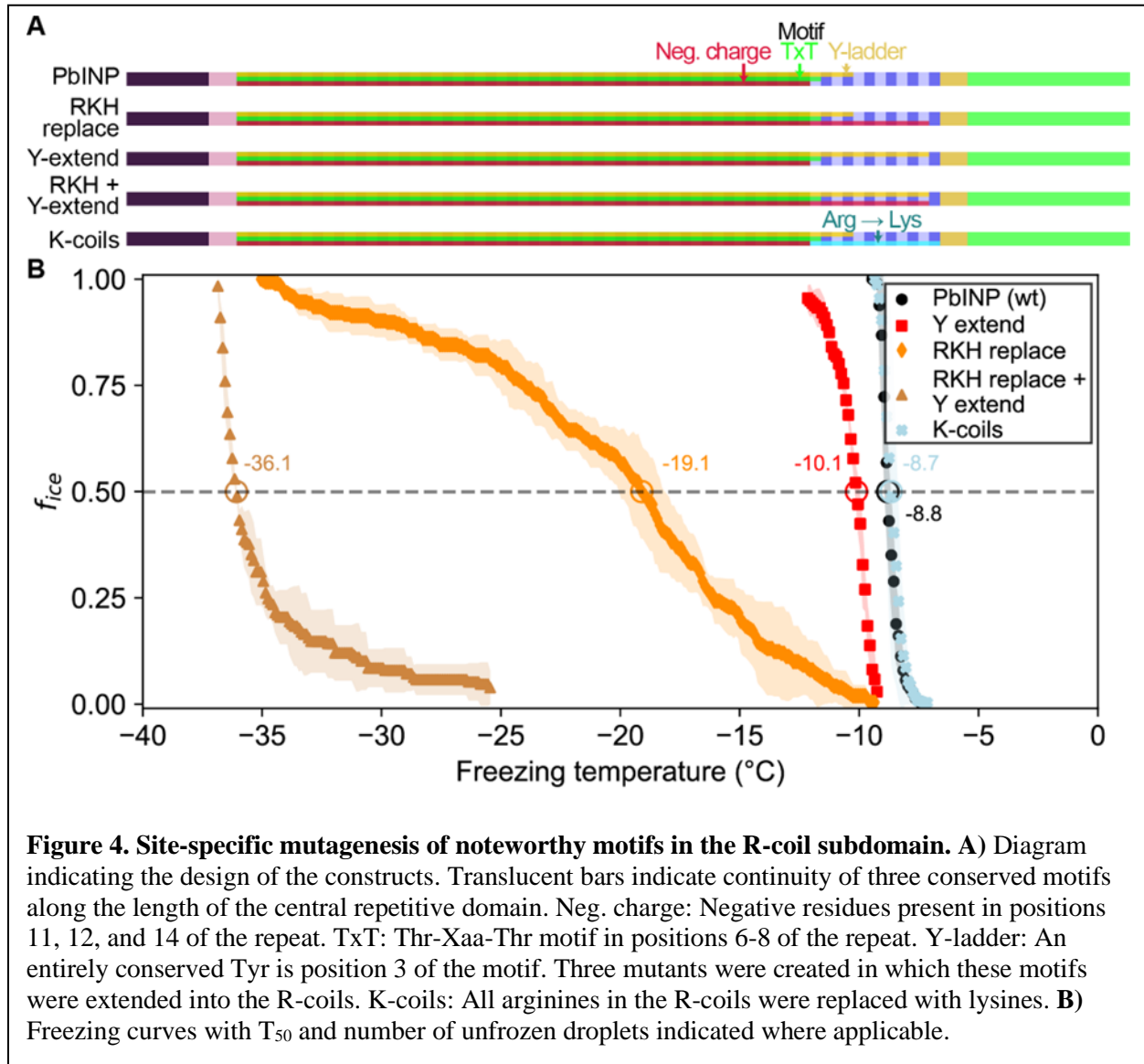


Figure 4. Site-specific mutagenesis of noteworthy motifs in the R-coil subdomain. A) Diagram indicating the design of the constructs. Translucent bars indicate continuity of three conserved motifs along the length of the central repetitive domain. Neg. charge: Negative residues present in positions 11, 12, and 14 of the repeat. TxT: Thr-Xaa-Thr motif in positions 6-8 of the repeat. Y-ladder: An entirely conserved Tyr is position 3 of the motif. Three mutants were created in which these motifs were extended into the R-coils. K-coils: All arginines in the R-coils were replaced with lysines. **B)** Freezing curves with T_{50} and number of unfrozen droplets indicated where applicable.

198

199

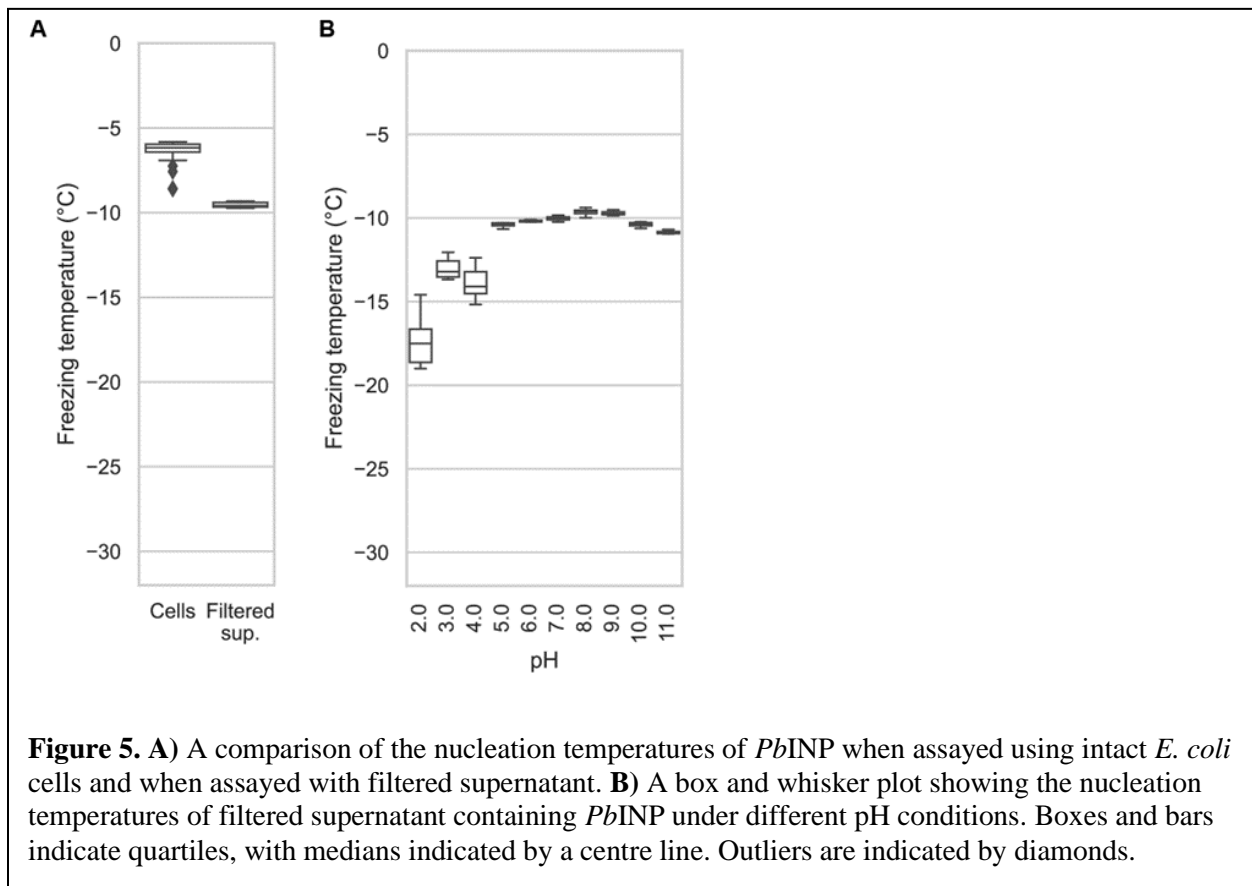
200 Droplet freezing assays show recombinant cell lysate supernatant has ice nucleation 201 activity that is affected by pH

202 The experiments described above were performed using whole recombinant bacteria rather than
203 extracted INPs. In *E. coli*, the vast majority of the expressed INP is intracellular (27). Indeed,
204 with our GFP-tagged constructs, we observe intense green fluorescence in the cytoplasm. To
205 study the effects of pH on *PbINP* activity, it was necessary to lyse the *E. coli* to change the pH
206 surrounding the INP multimers. After centrifuging the sonicate to remove cell debris and passing
207 the supernatant through a 0.2- μ m filter to remove any unbroken cells, the extracts were tested to

208 see how ice nucleation activity is affected by pH between 2.0 to 11.0. The activity of the filtered
209 supernatant was only a few degrees lower than that of whole bacteria ($T_{50} = -9.6\text{ }^{\circ}\text{C}$) (**Fig. 5A**),
210 which agrees with the results of Kassmannhuber *et al.* (28). This indicates that large INP
211 structures are present within the bacterial cytoplasm.

212

213 The effect of pH on Snomax activity has been previously reported (16). However, Snomax is
214 comprised of freeze-dried *P. syringae* cells in which the INPs are thought to be membrane
215 bound. Our assays on bacterial lysate tested free, cytoplasmic *Pb*INP complexes, producing a
216 similar trend regarding the effect of pH but with somewhat greater loss of activity on the lower
217 end of the optimal range (**Fig. 5B**). Ice nucleation activity decreased by a few degrees below pH
218 5.0, and by $\sim 8\text{ }^{\circ}\text{C}$ at pH 2.0. The loss of activity in the alkaline buffers up to pH 11.0 was
219 minimal. Similar to the findings of Chao *et al.* (30), we did not observe a major change in
220 activity (i.e. $\Delta T_{50} > 10\text{ }^{\circ}\text{C}$) even at the extremes of pH 2.0 and 11.0, suggesting that the
221 mechanism of ice nucleation is not pH-dependent.



222

223 **INP activity is remarkably heat resistant**

224 Having access to lysate also provided an opportunity to examine the heat stability of the INP
225 complexes. The filtered lysate was heat-treated to 60, 70, 80, 90, or 99 °C for 10 min in sealed
226 tubes before being chilled and assayed for ice nucleation activity (**Fig. 6A**). The activity of the
227 60 °C sample ($T_{50} = -9.9$ °C) was nearly identical to the non-treated wild-type control ($T_{50} = -9.6$
228 °C), and the 70 °C sample only displayed a minor loss of activity ($T_{50} = -10.2$ °C). From 80 °C to
229 99 °C the activity incrementally decreased ($T_{50} = -11.3$ °C, -12.7 °C, -14.6 °C, respectively), but
230 the activity loss never exceeded 6 °C. Indeed, the heat resistance of the INP complex is
231 remarkable. The C-terminal GFP tag provided an internal control for the effectiveness of heat
232 treatment, as GFP denatures at around 73 °C (31). The green colour of the bacteria was robust at
233 65 °C and with very few exceptions, gone at 75 °C (**Fig. 6B**). There was no fluorescence at 90
234 °C.

235

236 We also assayed the lysate of a construct from our previous study in which repeats 16-47
237 (residues 411-923) of the solenoid had been deleted, leaving 32 coils (6). The overall freezing
238 profile remained the same, indicating that this construct is also extremely resistant to heat
239 denaturation, with each temperature sample freezing at slightly lower temperatures than their
240 full-length counterparts (Fig. 6A). While the $\Delta 411-923$ construct had slightly lower overall
241 activity, its heat resistance was not affected by the truncation.

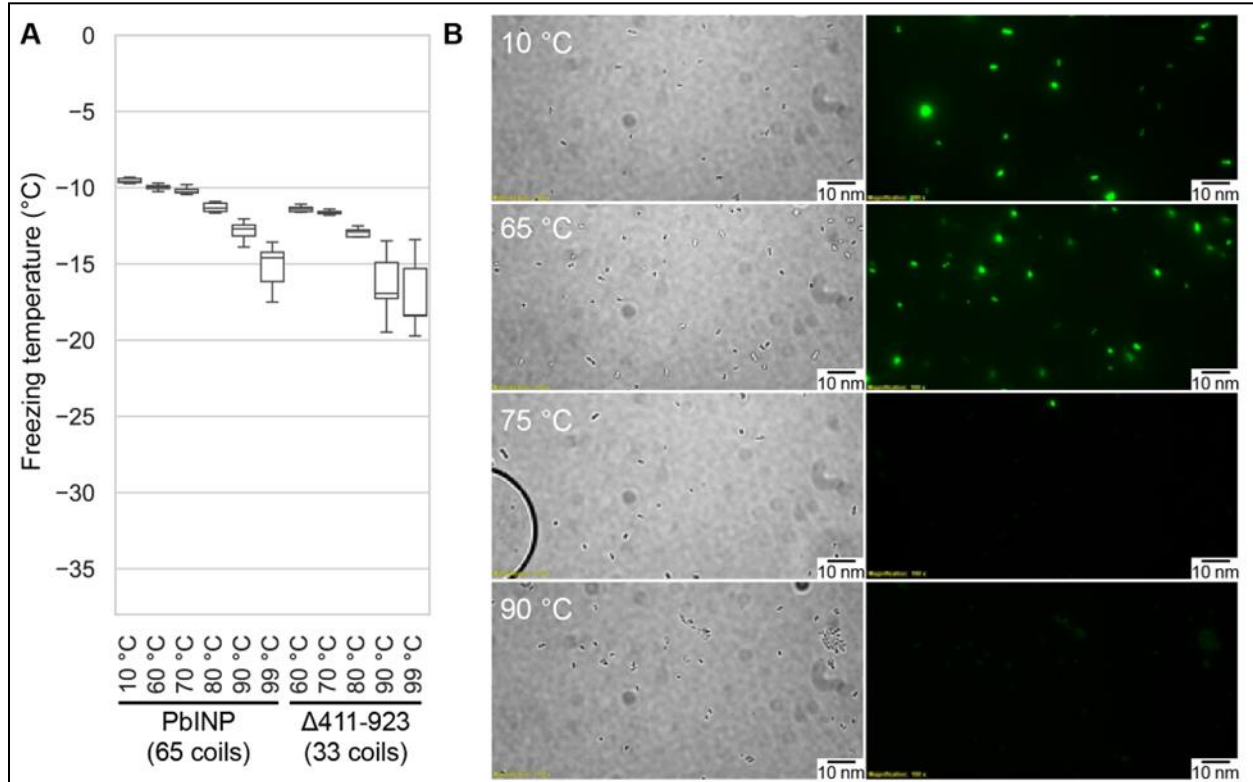


Figure 6. **A)** Measured freezing temperatures of heat-treated droplets containing either *PbINP* or *PbINP* with the first 32 repeats (counting from the N-terminal end) deleted. Wild-type *PbINP* freezing without heat treatment (kept at roughly 10 °C) is indicated- on the left. **B)** Fluorescent microscopy images of recombinant *E. coli* cells expressing *PbINP* tagged with GFP viewed under bright-field (BF) or fluorescent excitatory (GFP) light. Representative images are shown (n = 3). Note: cells that retain their fluorescence after 75 °C treatment are rarely observed.

243 **The β -solenoid of INPs is stabilized by a capping structure at the C terminus, but not at the**
244 **N terminus**

245 There is a clear C-terminal capping structure in the AlphaFold model (**Fig. 1A**), but a possible N-
246 terminal cap was more nebulous. Most protein solenoids are N- and/or C-terminally capped to
247 help maintain the fold and/or prevent end-to-end associations (32). Looking at the N-terminal
248 sequence, we tested if any part of the extended linker region serves as an N-terminal capping
249 motif. To investigate this, we made a series of incremental N-terminal deletions starting at
250 residues Asp150 (Truncation 1), Gln159 (Truncation 2), and Gln175 (Truncation 3) (**Fig. 7A**).
251 Truncation 1 lacked most of the N-terminal domain, leaving the last few residues of the
252 unstructured linker. Truncation 2 removed those linker residues so that the putative cap (a single
253 β -strand) was located at the very N-terminal end of the protein. Truncation 3 removed the β -
254 strand along with the rest of the first coil of the solenoid. When tested, there was no difference
255 between the activities of the three truncations and the wild type ($p = 0.82$ by one-way ANOVA)
256 (**Fig. 7D**). This result is in line with those from Kassmannhuber *et al.* (28), which showed that
257 deletion of the N-terminal domain does not significantly affect ice nucleation activity.

258
259 Previously, we demonstrated that the C-terminal cap is essential for ice nucleation activity (6).
260 Bioinformatic analysis showed a high degree of conservation in the C-terminal cap residues (**Fig.**
261 **7B**). Rather than deleting the cap, we made targeted mutations: F1204D, D1208L, and Y1230D,
262 to disrupt the structure predicted by AlphaFold. These mutations were chosen based on the
263 putative role of the residues in the AlphaFold model. F1204 sits atop the final R-coil to cover its
264 hydrophobic core. D1208 helps to maintain a tight loop through strategic hydrogen bonds, and
265 Y1230 fills a gap in the surface of the cap (**Fig. 7C**). When comparing these selections to the
266 aligned C-terminal cap sequences, we see that all three residues are highly conserved. The
267 resulting triple mutant displayed greatly reduced activity ($T_{50} = -27.8$ °C).

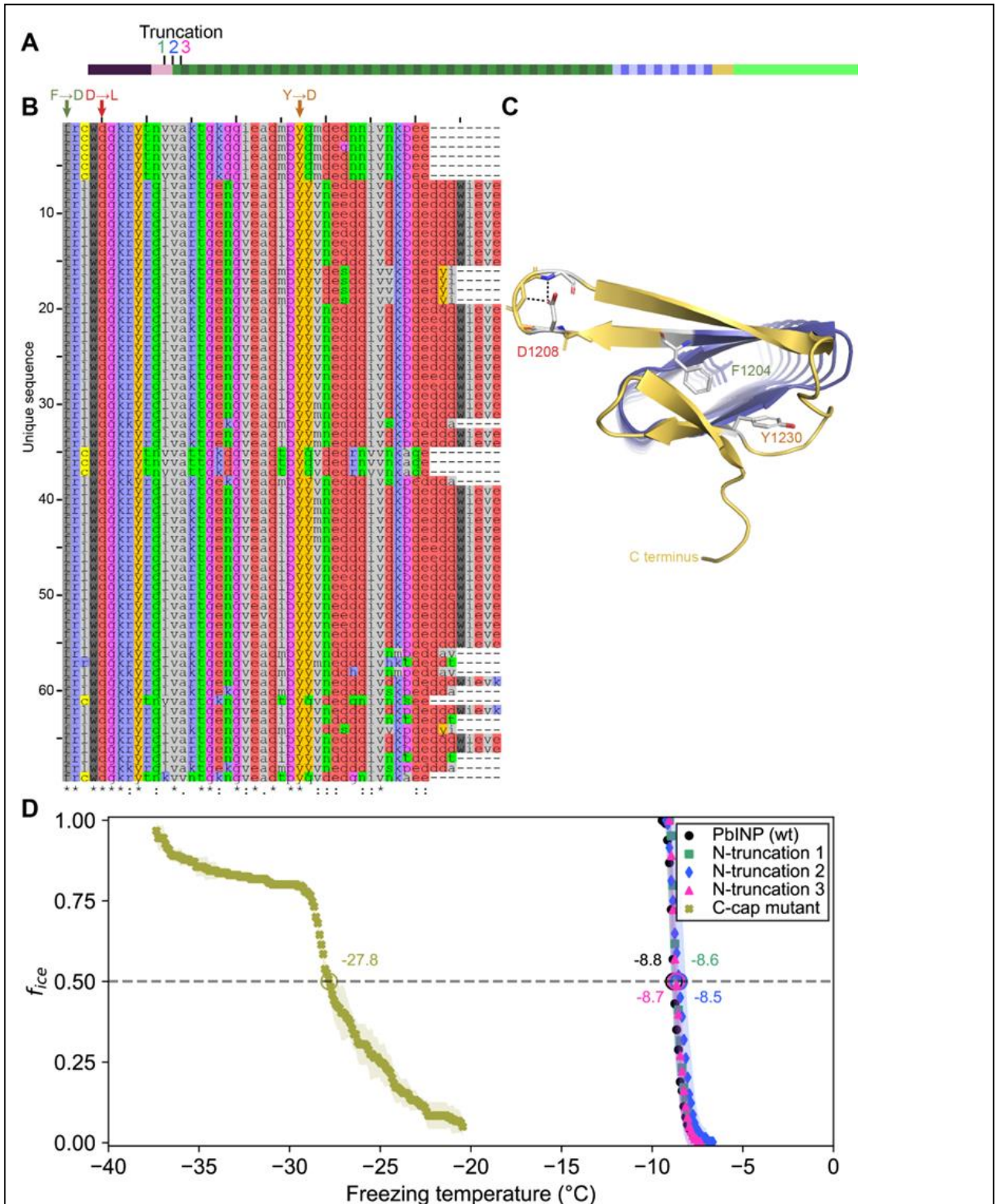


Figure 7. **A)** Sites of N-terminal truncations to *Pb*INP, indicating the location of the starting residue in the shortened construct. **B)** Alignment of representative INP C-terminal domains from the genus *Pseudomonas*. Mutated residues and their one-letter codes are indicated above. Symbols at the bottom indicate consensus (* for fully conserved, : for conservation of strongly similar chemical properties, . for conservation of weakly similar chemical properties). **C)** Predicted location of mutated residues in the *Pb*INP C-terminal cap with sidechains shown and predicted H-bonds for D1208 shown as dashed lines. **D)** The ice nucleation curves for the N- and C-terminal cap mutants.

269 Cryo-electron tomography reveals INPs multimers form bundled fibres in recombinant cells
270 *E. coli* cells recombinantly overexpressing INPs were plunge-frozen and milled into ~150-nm
271 thick lamella using cryo-FIB (**Fig. 8A**). Grids containing lamellae were transferred into either a
272 200- or a 300-kV transmission electron microscope for imaging under cryogenic conditions.
273 Many *E. coli* cells were observed within the low-magnification cryo-TEM overview image of the
274 lamella (**Fig. 8B**). Tilt series were collected near individual *E. coli* cells, and 3-D tomograms
275 were reconstructed to reveal cellular and extracellular features. Strikingly, *E. coli* cells
276 overproducing wild-type INPs appear to be lysed after 3 days of cold acclimation at 4 °C and
277 contain clusters of fibres in the cytoplasm (**Fig. 8 C, D, E**, tomograms in **Movies S2** and **S3**).
278 Individual fibres are up to a few hundred nanometers in length but only a few nanometers in
279 width. Intriguingly, these fibre clusters were not observed in those *E. coli* that overexpress INP
280 mutants lacking R-coils and the cell envelopes stay integral after being cold acclimated over the
281 same period as those of wild-type INP-producing *E. coli*. (**Fig. S5 A, B, C, D**).

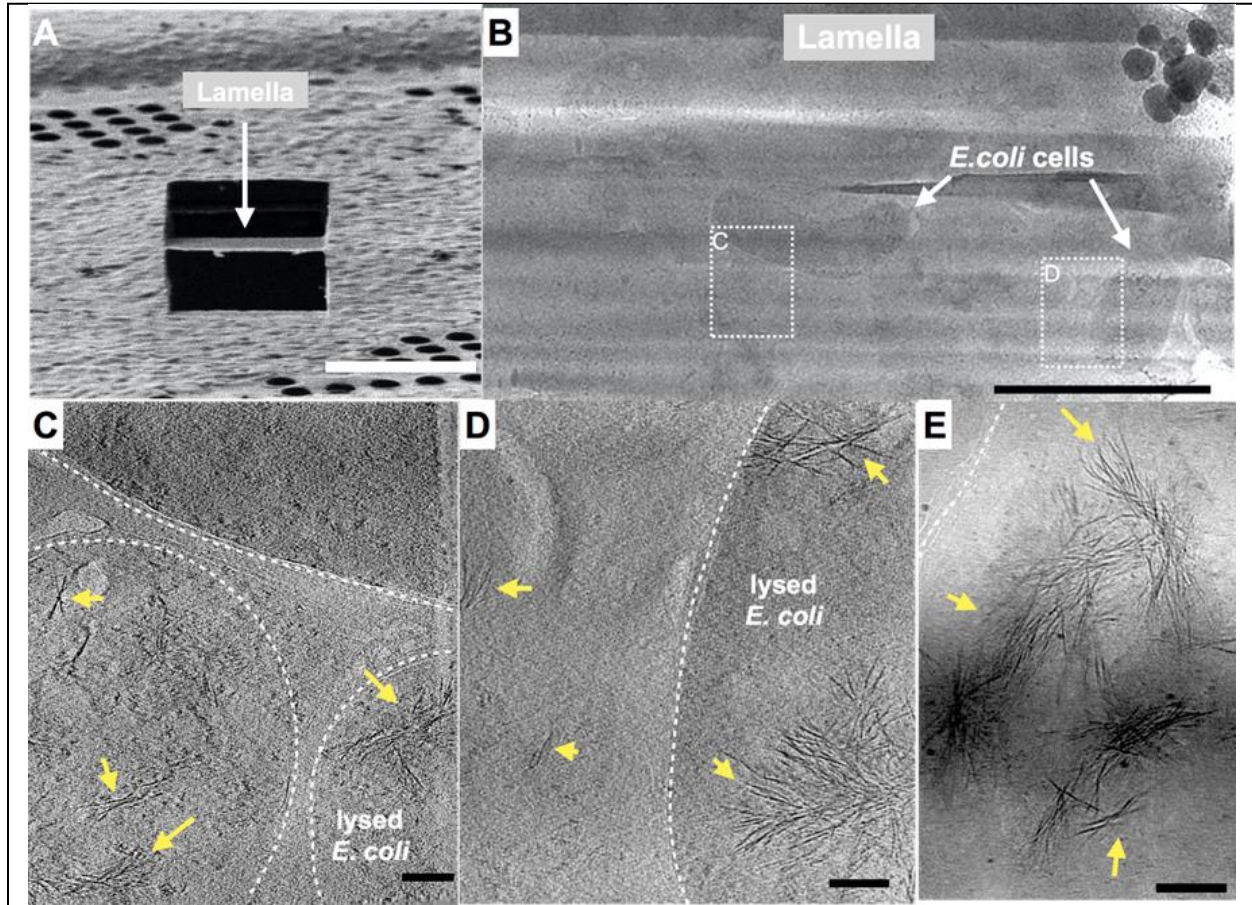


Figure 8. Fibrous bundles observed by cryo-FIB and cryo-ET in *E. coli* cells expressing INP.

A) Ion-beam image of a thin lamella containing *E. coli* cells expressing INP obtained from cryo-FIB milling. **B)** Zoomed-in view of a cryo-TEM image of the lamella in **A)**. Boxes with dashed-lines indicate areas where tilt series were collected. **C)** and **D)** Snapshots from 3-D cryo-tomograms reconstructed from tilt series collected in the boxed regions in **B)** showing striking fibrous bundles (yellow arrowheads). The *E. coli* cell envelopes are indicated with thick dash-lines. **E)** Further examples of the fibrous bundles produced by INP-expressing *E. coli*. Size markers in **A)** is 10 µm, in **B)** is 2 µm and in **C)**, **D)** and **E)** are 100 nm, respectively.

282

283

284 Discussion

285 Previously, we showed that the PbINP solenoid domain is made up of two subdomains: the
286 larger N-terminal region of WO-coils accounting for 80-90% of the total length; and the smaller
287 C-terminal R-coil region accounting for the remaining 10-20% (6). The length of the WO-coil
288 region and the continuity of the water-organizing motifs were shown to directly affect ice
289 nucleation temperature. Although the R-coil region lacks water-organizing motifs, its presence
290 was critical for ice nucleation activity, which led us to propose a key role for this region in INP

291 multimer formation. Here we have characterized the R-coil subdomain in terms of the attributes
292 it needs to support INP multimerization and have shown by cryo-ET the first *in situ* view of what
293 these multimers look like. In addition, we have advanced a working model for the INP multimer
294 structure that is compatible with all of the known INP properties.

295
296 Removal of the front or middle halves of the PbINP solenoid (leaving 33 coils) only dropped the
297 ice nucleation activity by ~ 2 °C. In these experiments, the R-coils were not shortened, so these
298 deletions caused a disproportional loss of WO-coils from 53 to 21. Here we have confirmed this
299 tolerance of WO-coil count variation through bioinformatic analysis of natural INPs. The
300 majority of bacterial INPs have WO-coil counts ranging from ~ 30 to 70. *PbINP* is average in this
301 respect with 53 WO-coils.

302
303 It seems counterintuitive that these bacteria have not been uniformly selected for the highest
304 WO-coil count, which might give them an advantage in causing frost damage to plants at the
305 highest possible temperature (33). However, it is clear that INPs are not functioning as
306 monomers but rather as large multimers. Thus, any loss of length can potentially be compensated
307 for by adding more monomers to the multimer. The ability to form these superstructures is a key
308 property of the INPs and centers on the R-coil subdomain. This was shown in the same
309 bioinformatic analysis where there is remarkably little variation to the R-coil length of 10-12
310 coils. The importance of a minimal R-coil length is supported here by experiments. Whereas
311 over 50% of the WO-coils can be removed with minimal loss of activity, when six of the 12
312 *PbINP* R-coils were replaced by WO-coils there was a catastrophic loss of ice nucleation
313 activity, and no activity at all with further shortening of the R-coils. We postulate that at least
314 eight R-coils are required for efficient multimer formation and that the ice nucleation activity of
315 a monomer is inconsequential in the natural environment.

316
317 In the absence of detailed structural information, we have probed the properties of the multimers
318 to help develop feasible models for their structure and assembly. The location of the R-coils at
319 the C-terminal end of the solenoid next to the highly conserved cap structure is critical, as they
320 do not function in the middle of the WO-coil region, and only poorly at the N-terminal end.
321 These R-coils have a strong positive charge from the Arg and Lys residues, whereas the WO-

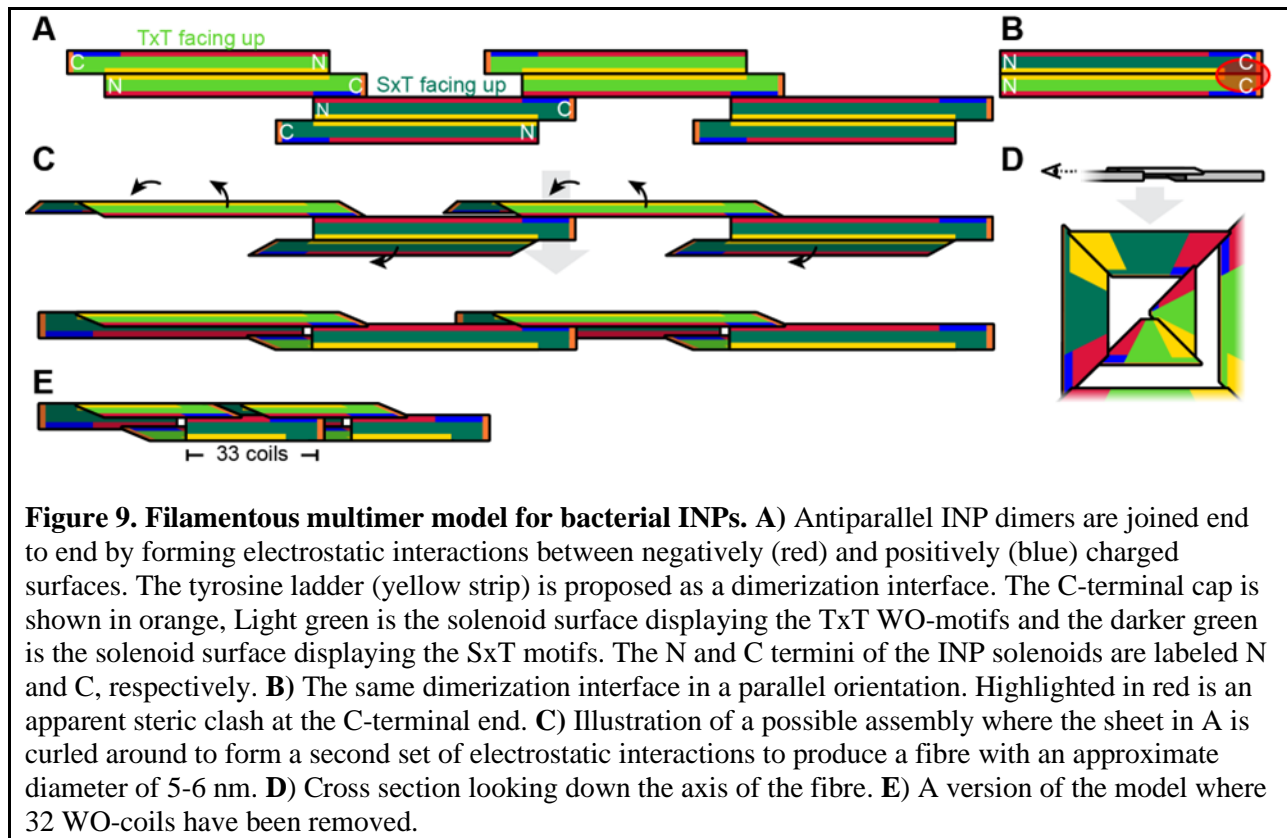
322 coils are negatively charged, and their interaction potentially provides an electrostatic component
323 to the fibre assembly. In this regard, the negative charges of the WO-coils are consistent
324 throughout their length, which offers no clue as to where on the WO-coils the R-coils might
325 interact. One possible advantage of this uniformity is that multimer assembly could still happen
326 if the WO-coil length is appreciably shortened.

327

328 As expected, changing the charge on the R-coils from positive to negative caused a large loss of
329 ice nucleation activity of ~ 9 °C, consistent with charge repulsion between these two solenoid
330 regions. The minimal effects of pH on native INP activity are reminiscent of the insensitivity of
331 antifreeze activity to pH (30, 34). The ice-binding sites of AFPs are typically devoid of charged
332 residues and there should be no effect of pH on the ability of these sites to organize ice-like
333 waters. The same can be said for the water-organizing motifs in INPs. Any effect of pH on ice-
334 binding or ice-nucleating activity is likely due to changes to the protein fold or INP multimer.
335 The small effect of pH on INP activity encouraged us to consider other possible interactions in
336 the assembly of multimers. We noted the extraordinary heat stability of INP multimers. Even
337 after heating to 99 °C for 10 min the bacterial extracts only lost 5 °C of ice nucleation activity,
338 whereas the heat-stable internal GFP control was denatured at 75 °C. We cannot rule out the
339 possibility that the INP multimers were also denatured by heat treatment but could reassemble on
340 cooling.

341

342



343

344 **Figure 9. Filamentous multimer model for bacterial INPs.** **A)** Antiparallel INP dimers are joined
345 to end by forming electrostatic interactions between negatively (red) and positively (blue) charged
346 surfaces. The tyrosine ladder (yellow strip) is proposed as a dimerization interface. The C-terminal cap
347 is shown in orange, Light green is the solenoid surface displaying the TxT WO-motifs and the darker green
348 is the solenoid surface displaying the SxT motifs. The N and C termini of the INP solenoids are labeled N
349 and C, respectively. **B)** The same dimerization interface in a parallel orientation. Highlighted in red is an
350 apparent steric clash at the C-terminal end. **C)** Illustration of a possible assembly where the sheet in A is
351 curled around to form a second set of electrostatic interactions to produce a fibre with an approximate
352 diameter of 5-6 nm. **D)** Cross section looking down the axis of the fibre. **E)** A version of the model
353 where 32 WO-coils have been removed.

354 Working model of the INP multimer

355 The fundamental unit of the INP multimer in this hypothetical model is a dimer (**Fig. 9**). The
356 dimerization interface involves an interaction of the stacked tyrosine ladders (coloured yellow in
357 **Fig. 9A**) from the two INP monomers as previously suggested (8, 22). However, in this model
358 the INPs are aligned antiparallel to each other (**Fig. 9B**). This orientation is more likely than a
359 parallel alignment since the R-coils and C-terminal cap structure appear to clash when modelled
360 (**Movie S4**). The antiparallel dimer would not be a rigid flat sheet but could hinge at the tyrosine
361 ladder. Another advantage of the antiparallel arrangement is that the two dimer termini are
362 identical allowing end-to-end linking to form a long fibre.

363

364 The end-to-end dimer associations involve electrostatic interactions between the basic side of the
365 R-coils and the acidic side of the WO-coils (**Fig. 9A**). If these interactions also form a hinge, it
366 should be possible to roll the end-linked dimers into a compact fibre (**Fig. 9C**) with a diameter
367 close to that seen by cryo-ET (**Fig. 8**). At the dimer ends where the R-coils form an electrostatic

368 interaction with the far end of the WO-coils there are two sets of interacting surfaces involved in
369 making the rolled up fibre. The antiparallel arrangement of the dimers gives a sidedness to the
370 multimer where TxT motifs (light green) face outwards and inwards in an alternating pattern
371 with SxT motifs (dark green) in the opposite phase. A cross-sectional view of the INP fibre (**Fig.**
372 **9D**) shows the alternating water-organizing surfaces, the interactions between the negatively
373 (red) and positively (blue) charged regions, and the openness of the structure to organize ice-like
374 water molecules inside and outside of the fibre.

375

376 In addition, the additional stabilizing interfaces offered by this assembly would further stabilize
377 the multimer into a rigid fibre and also help to explain the apparent heat resistance of INP
378 samples.

379

380 **Working model of the INP multimer is consistent with the properties of INPs and their**
381 **multimers.**

382 We previously showed that the length of the WO-coil region can be shortened by ~60% with
383 only a few °C decrease in ice nucleation temperature (6). The working model can accommodate
384 these huge deletions simply by closing the gap between the dimers. For example, the deletion of
385 32 WO-coils, leaving just 21 and the 12 R-coils (**Fig. 9E**) retains all the molecular interactions
386 seen in the longer fibre but with fewer stacked tyrosine interactions. This can help explain the
387 heat stability of the INP multimers and the minimal difference (2-3 °C) in activity loss between
388 full-length *Pb*INP with 65 coils and the truncated version with 33 coils (**Fig. 6**). Similarly, longer
389 WO-coil regions can be accommodated by lengthening the gap. This can explain the wide range
390 of WO-coil lengths seen in nature (**Fig. 2**). They all fit in the same model.

391

392 Our model also shows how the interaction between the R-coils and the WO-coils of the adjacent
393 dimers supports fibre formation. Any shortening of the R-coil subdomain jeopardizes the ability
394 to link up the dimers. The catastrophic loss of ice nucleation activity seen below 8 R-coils is
395 because the interacting length of R-coils and WO-coils has too few electrostatic and other
396 interactions to bridge the dimers together. The importance of electrostatic interaction has been
397 illustrated in this study in two ways. When the R-coil basic residues were replaced by acidic
398 residues, the ice nucleation activity was severely compromised but was fully restored when the

399 mutated residues were all converted to lysines. Additionally, in cell-free extracts of lysed INP-
400 producing *E. coli* ice nucleation activity decreased by a few degrees Celsius at low pH values
401 where the charge on acidic residue side chains was reduced or eliminated. When the carboxyl
402 groups of aspartate and glutamate involved in electrostatic pairing lose their negative charges at
403 low pH they can still form hydrogen bonds with basic amino acid partners, which can explain
404 why the lowering of pH was not as disruptive as reversing the charge on these residues.
405 The observation that low, variable levels of ice nucleation activity remained in the construct
406 where the R-coil basic residues were replaced by acidic residues, suggests that there are
407 additional binding interactions between the dimers other than electrostatic ones. Here we suggest
408 the involvement of the highly conserved C-terminal capping structure. When three mutations
409 designed to disrupt the cap fold were introduced all ice nucleation activity was lost. Also of note
410 is the disruptive effect of extending the tyrosine ladder further into the R-coil sub-domain in the
411 mutant where the acidic residues replaced the basic one. The subtle details of the R-coil region
412 will require detailed structural analysis for their elucidation.

413
414 The relocation of the R-coils to the N-terminal end of the solenoid caused a loss of just over 50%
415 activity and it is possible to accommodate such a change in the model while retaining a charge
416 interaction between the R-coils and WO-coils. However, the separation from the cap structure
417 might account for some of the activity loss. Movement of the R-coils to the centre of the WO-
418 coil region is not compatible with the model and sure enough this construct was devoid of ice
419 nucleation activity (**Fig. 3B**).

420
421 Other features supporting the model are that the dimer's C- and N-terminal ends are exposed and
422 can accommodate tags and extensions without disrupting the fibre. Thus, the addition of a C-
423 terminal GFP tag has no detrimental effect in ice nucleation activity. Nor is there any difference
424 in activity if the N-terminal INP domain and linker region are present or not (**Fig. 7**) (6, 28).
425 Even the incorporation of bulky mRuby into the WO-coils (6) can be accommodated because the
426 fibre is too thin for the solenoids to be packed together in a bundle.

427
428 Electron microscopy of newly synthesized INPs in a cell-free system shows them as thin
429 molecules of dimensions 4-6 nm in diameter by a few hundred nm in length (23). Negatively

430 stained images of recombinantly produced INP multimers isolated by centrifugation and
431 chromatography show an elongated structure ~5-7 times longer than a monomer but not much
432 wider (22). The fibres seen *in situ* in INP-expressing *E. coli* (**Fig. 8**) are similarly long but
433 slightly thinner, consistent with the absence of negative staining. The model in **Fig. 9** is the
434 thinnest structure we can project for a fibrillar multimer.

435

436 Solving the structure of the INP fibres at atomic detail will be the key to understanding the
437 remarkable ability of biological ice nucleators to start the freezing process at high sub-zero
438 temperatures. Structures of this type offer the promise of cell-free ice nucleation for use in
439 biotechnological and food applications where there is a need to avoid the use of bacteria.

440

441 **Methods**

442 **AlphaFold prediction**

443 The AlphaFold model for *Pb*INP was generated by Forbes *et al.* as described (6).

444

445 **Bioinformatic analysis of INPs**

446 NCBI's BLAST was accessed using the BioPython library v1.81 (35). The consensus sequence
447 for the 16-residue coil 'AGYGSTQTAGEDSSLT' was used as the query against the non-
448 redundant (nr) database. The PAM30 scoring matrix was used due to the short query.

449 Quality control (QC) was performed using custom Python scripts, making use of BioPython's
450 Entrez module to fetch information on the protein, BioProject, and assembly method for each
451 BLAST result (**Fig. S1**). Custom Python scripts were used to automatically identify the tandem
452 repeats and classify them as WO-coils or R-coils.

453 Sequence logos were made using the Logomaker package v0.8 (36). Alignment of C-terminal
454 cap sequences was performed using JalView software v2.11.2.6 (37).

455

456 **Synthesis of *Pb*INP genes**

457 Experiments for this project used a synthetic *Pb*INP gene previously developed by our group.

458 This codon-optimized gene encodes the *P. borealis* INP gene (GenBank accession: [EU573998](#)).

459 Additionally, the DNA sequence for enhanced green fluorescent protein (eGFP) (GenBank

460 accession: [AAB02572](#)) was fused to the 3'-end of the *PbINP* gene using a hexanucleotide
461 encoding two linker residues (Asn-Ser). More details about the *PbINP*-eGFP sequence are
462 provided in Forbes *et al.* (6).

463
464 All mutants for this study were designed by modifying the aforementioned synthetic gene.
465 GenScript performed all (Piscataway, NJ, USA) gene syntheses, which we subsequently cloned
466 into the pET-24a expression vector.

467
468 Five *PbINP* mutants were designed to test the effect of replacing the R-coils. The R-coils were
469 incrementally replaced with the sequences of WO-coils adjacent to the R-coil region as
470 indicated, resulting in constructs containing 10, 8, 6, 4, and 1 R-coil (**Fig. 2A**). Replacements
471 were designed such that they maintained the periodicity of the tandem repeats. The C-terminal
472 R-coil was left untouched to avoid disturbing possible interactions with the putative C-terminal
473 cap structure.

474
475 The R-coils were either relocated within the protein or deleted (**Fig. 3A**), while again leaving the
476 N- and C-terminal coils untouched to avoid interactions with adjacent domains.

477
478 Targeted mutations were introduced to the R-coil region gene to produce four additional
479 constructs (**Fig. 4A**). For the first construct (RKH replacement), any positively charged residues
480 (Arg, Lys, His) in positions 11, 12, or 14 in the R-coils were replaced with residues commonly
481 found in those locations in the WO-coils (Asp, Glu, and Gly for positions 11 and 12, Ser for
482 position 14). The second construct Y extend in **Fig. 4A** extends the stacked tyrosine ladder
483 present at position 3 of the coils through 7 additional coils toward the C terminus of the solenoid.
484 The third construct (RKH replacement + Y extend in **Fig. 4A** is a combination of both mutants.
485 The fourth construct (K-coils in **Fig. 4A**) converted every Arg residue in the R-coil section to a
486 Lys residue.

487
488 **Protein expression in *E. coli***

489 Each *PbINP* construct was transformed into the ArcticExpress strain of *E. coli*, since its
490 expression of two cold-adapted chaperones, Cpn10 and Cpn60, promotes the correct folding of

491 proteins at low temperatures (38). Transformation and induction with IPTG were performed
492 according to the supplier's instructions (Agilent Technologies, Catalog #230192). Cells
493 expressed at 10 °C for 24 h post-induction. The eGFP tag allowed expression to be confirmed
494 using fluorescence microscopy (6).

495

496 **Ice nucleation assays by WISDOM**

497 Constructs were assayed on WISDOM (Weizmann Supercooled Droplets Observation on a
498 Microarray) (39) in a similar way as described in Forbes *et al.* (6).

499

500 **Ice nucleation assays by nanoliter osmometer**

501 Ice nucleation activity was quantified using a droplet freezing assay protocol (Lee *et al.*,
502 submitted) that makes use of a LabVIEW-operated nanoliter osmometer (Micro-Ice, Israel) (40).
503 Briefly: Following induction and cold incubation, nanoliter-sized droplets of liquid cultures were
504 pipetted into oil-filled wells resting on a cold stage. The temperature of the cold stage was
505 lowered at a rate of 1 °C per minute while a video recording was taken of the sample grid.
506 Freezing was characterized by a distinct change in droplet appearance. After assay completion,
507 the videos were analyzed to record the temperatures of all freezing events. The fraction of frozen
508 droplets (f_{ice}) as a function of temperature was plotted, generating ice nucleation curves for each
509 sample. This apparatus could not reach temperatures as low as those achieved on WISDOM, but
510 results are in agreement between the two approaches (**Fig. 2B**).

511

512 **Heat treatment and pH**

513 To obtain cell lysates, *E. coli* cultures were centrifuged at $3,200 \times g$ for 30 min post-induction.
514 Cell pellets were then resuspended in a lysis buffer of 50 mM Tris-HCl, 150 mM NaCl,
515 containing Pierce Protease Inhibitor (Thermo Scientific, Canada) before sonication at 70%
516 amplitude for 30-s rounds. Lysate was centrifuged at $31,000 \times g$ and the resulting supernatant
517 was passed through a 0.2 μm filter.

518

519 For heat treatment, filtered lysate in sealed Eppendorf tubes was heated at 60 °C, 70 °C, 80 °C,
520 90 °C, or 99 °C for 10 min in a thermocycler and then quenched on ice prior to being assayed for
521 activity.

522
523 For the pH experiments, aliquots of filtered lysate were diluted 50-fold in pH-adjusted buffer of
524 100 mM sodium citrate, 100 mM sodium phosphate, and 100 mM sodium borate following the
525 protocol by Chao *et al.* (30). Before assaying, we verified using universal indicator strips that
526 addition of lysate to the buffer mixtures did not meaningfully affect the pH of the final mixtures.

527

528 **Preparation of the cryo-EM grids**

529 After confirming eGFP-INP expression, the *E. coli* cultures were incubated at 4 °C for an
530 additional 3 days. The *E. coli* cells were spun down and resuspended in PBS to an OD_{600 nm} of
531 ~ 3. These concentrated *E. coli* samples were deposited onto freshly glow-discharged
532 QUANTIFOIL holey carbon grids (Electron Microscopy Sciences). The grids were then blotted
533 from the back side with the filter paper for ~5 s before plunge-frozen in liquid ethane, using a
534 manual plunger-freezing apparatus as described previously (41, 42).

535

536 **Cryo-FIB milling**

537 The plunge-frozen grids with *E. coli* cells were clipped into cryo-FIB AutoGrids and mounted
538 into the specimen shuttle under liquid nitrogen. An Aquilos2 cryo-FIB system (Thermo Fisher
539 Scientific) was used to mill the thick bacterial samples into lamellae of < 200 nm in thickness.
540 The milling process was completed using a protocol as previously described (43).

541 **Cryo-ET data acquisition and tomogram reconstruction**

542 Grids containing the lamellae obtained from cryo-FIB milling were loaded into either a 300-kV
543 Titan Krios electron microscope (Thermo Fisher Scientific) equipped with a Direct Electron
544 Detector and energy filter (Gatan) or a 200-kV Glacios Electron Microscope at Yale University.
545 The FastTOMO script was used with the SerialEM software to collect tilt series with defocus
546 values of approximately $-6 \mu\text{m}$ (44), and a cumulative dose of $\sim 70 \text{ e}^-/\text{\AA}$ covering angles from
547 -48° to 48° (3° tilt step). Images were acquired at $42,000 \times$ magnification with an effective pixel

548 size of 2.148 Å. All recorded images were first drift corrected by MotionCor2 (45), stacked by
549 the software package IMOD (46), and then aligned by IMOD using Pt particles as fiducial
550 markers. TOMO3D was used to generate tomograms by simultaneous iterative reconstruction
551 technique (SIRT) (47). In total, 10 tomograms were reconstructed with TOMO3D for the WT
552 INP while 5 tomograms were produced for the R-coil mutant.

553 **Data Availability**

554 The full dataset of long-read sequences used is available in **Supplementary Data 1**.

555

556 **Contributions**

557 T.H., J.C.L., and P.L.D. planned these experiments based on the identification of the R-coil
558 subdomain by T.H. and P.L.D. in a prior work. T.H., J.C.L., and P.L.D. wrote the original
559 manuscript for peer review. T.H. and P.L.D. designed the model for multimerization. T.H. coded
560 the pipeline and performed the bioinformatic analysis of INPs.

561

562 T.H. and J.C.L. designed all mutants and prepared all samples except where otherwise noted.
563 J.C.L. prepared the buffers and samples for the pH experiments, and performed all measurements
564 of ice nucleation activity on the nanoliter osmometer. T.H. and J.C.L. performed the heat
565 treatment experiments.

566

567 G.O. and I.B. prepared samples whose activity was assayed by N.R. and Y.R. on WISDOM.
568 S.G., W.G. and J.L. performed cryo-FIB and cryo-ET experiments. S.G. prepared Fig. 8 and
569 Movies S2 and S3. T.H. prepared all other figures.

570

571 **Acknowledgements**

572 This work was supported by CIHR Foundation Grant FRN 148422 to P.L.D., who holds the
573 Canada Research Chair in Protein Engineering, and by an Israel Science Foundation grant to I.B.
574 YR acknowledges support by a research grant from the Yotam project and the Weizmann
575 institute sustainability and energy research initiative. S.G. was supported by a CIHR Post-
576 Doctoral Fellowship and an NIH RO1 grant (R01AI087946) of J.L. W.G. was also supported by

577 the NIH RO1 grant (R01AI087946) of J.L. We thank Virginia K. Walker for the gift of the
578 *Pseudomonas borealis* strain.
579

580 References

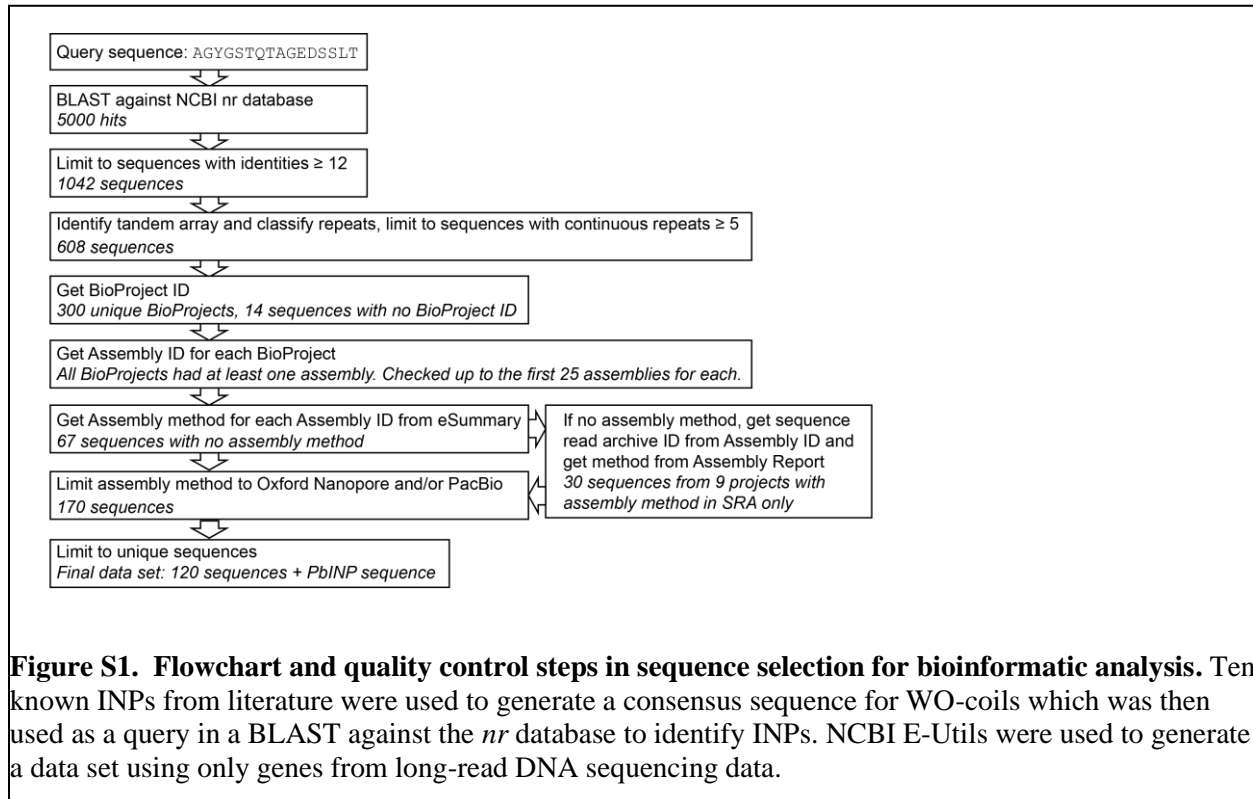
- 581 1. Hoose, C., and Möhler, O. (2012) Heterogeneous ice nucleation on atmospheric aerosols: a
582 review of results from laboratory experiments *Atmospheric Chemistry and Physics* **12**, 9817-
583 9854 <http://dx.doi.org/10.5194/acp-12-9817-2012>
- 584 2. Vali, G., DeMott, P. J., Möhler, O., and Whale, T. F. (2015) Technical Note: A proposal for ice
585 nucleation terminology *Atmospheric Chemistry and Physics* **15**, 10263-10270
586 <http://dx.doi.org/10.5194/acp-15-10263-2015>
- 587 3. Lukas, M., Schwidetzky, R., Eufemio, R. J., Bonn, M., and Meister, K. (2022) Toward
588 Understanding Bacterial Ice Nucleation *J Phys Chem B* **126**, 1861-1867
589 <http://dx.doi.org/10.1021/acs.jpcc.1c09342>
- 590 4. Govindarajan, A. G., and Lindow, S. E. (1988) Size of bacterial ice-nucleation sites measured in
591 situ by radiation inactivation analysis *Proc Natl Acad Sci U S A* **85**, 1334-1338
592 <http://dx.doi.org/10.1073/pnas.85.5.1334>
- 593 5. Lindow, S. E., Lahue, E., Govindarajan, A. G., Panopoulos, N. J., and Gies, D. (1989) Localization of
594 ice nucleation activity and the iceC gene product in *Pseudomonas syringae* and *Escherichia coli*
595 *Mol Plant Microbe Interact* **2**, 262-272 <http://dx.doi.org/10.1094/mpmi-2-262>
- 596 6. Forbes, J., Bissoyi, A., Eickhoff, L., Reicher, N., Hansen, T., Bon, C. G. *et al.* (2022) Water-
597 organizing motif continuity is critical for potent ice nucleation protein activity *Nat Commun* **13**,
598 5019 <http://dx.doi.org/10.1038/s41467-022-32469-9>
- 599 7. Graether, S. P., and Jia, Z. (2001) Modeling *Pseudomonas syringae* ice-nucleation protein as a
600 beta-helical protein *Biophys J* **80**, 1169-1173 [http://dx.doi.org/10.1016/S0006-3495\(01\)76093-6](http://dx.doi.org/10.1016/S0006-3495(01)76093-6)
- 601 8. Garnham, C. P., Campbell, R. L., Walker, V. K., and Davies, P. L. (2011) Novel dimeric beta-helical
602 model of an ice nucleation protein with bridged active sites *BMC Struct Biol* **11**, 36
603 <http://dx.doi.org/10.1186/1472-6807-11-36>
- 604 9. Graether, S. P., Kuiper, M. J., Gagne, S. M., Walker, V. K., Jia, Z., Sykes, B. D. *et al.* (2000) Beta-
605 helix structure and ice-binding properties of a hyperactive antifreeze protein from an insect
606 *Nature* **406**, 325-328 <http://dx.doi.org/10.1038/35018610>
- 607 10. Graham, L. A., Qin, W., Loughheed, S. C., Davies, P. L., and Walker, V. K. (2007) Evolution of
608 hyperactive, repetitive antifreeze proteins in beetles *J Mol Evol* **64**, 387-398
609 <http://dx.doi.org/10.1007/s00239-005-0256-3>
- 610 11. Kristiansen, E., Ramlov, H., Hojrup, P., Pedersen, S. A., Hagen, L., and Zachariassen, K. E. (2011)
611 Structural characteristics of a novel antifreeze protein from the longhorn beetle *Rhagium*
612 *inquisitor* *Insect Biochem Mol Biol* **41**, 109-117 <http://dx.doi.org/10.1016/j.ibmb.2010.11.002>
- 613 12. Garnham, C. P., Campbell, R. L., and Davies, P. L. (2011) Anchored clathrate waters bind
614 antifreeze proteins to ice *Proc Natl Acad Sci U S A* **108**, 7363-7367
615 <http://dx.doi.org/10.1073/pnas.1100429108>
- 616 13. Green, R. L., and Warren, G. J. (1985) Physical and functional repetition in a bacterial ice
617 nucleation gene *Nature* **317**, 645-648 <http://dx.doi.org/10.1038/317645a0>

- 618 14. Kajava, A. V., and Steven, A. C. (2006) The turn of the screw: variations of the abundant beta-
619 solenoid motif in passenger domains of Type V secretory proteins *J Struct Biol* **155**, 306-315
620 <http://dx.doi.org/10.1016/j.jsb.2006.01.015>
- 621 15. Madzharova, F., Bregnhøj, M., Chatterley, A. S., Lovschall, K. B., Drace, T., Andersen Dreyer, L. S.
622 *et al.* (2022) Electrostatics Trigger Interfacial Self-Assembly of Bacterial Ice Nucleators
623 *Biomacromolecules* **23**, 505-512 <http://dx.doi.org/10.1021/acs.biomac.1c01217>
- 624 16. Lukas, M., Schwidetzky, R., Kunert, A. T., Poschl, U., Frohlich-Nowoisky, J., Bonn, M. *et al.* (2020)
625 Electrostatic Interactions Control the Functionality of Bacterial Ice Nucleators *J Am Chem Soc*
626 **142**, 6842-6846 <http://dx.doi.org/10.1021/jacs.9b13069>
- 627 17. Schwidetzky, R., Lukas, M., YazdanYar, A., Kunert, A. T., Poschl, U., Domke, K. F. *et al.* (2021)
628 Specific Ion-Protein Interactions Influence Bacterial Ice Nucleation *Chemistry* **27**, 7402-7407
629 <http://dx.doi.org/10.1002/chem.202004630>
- 630 18. Juurakko, C. L., diCenzo, G. C., and Walker, V. K. (2022) Brachypodium Antifreeze Protein Gene
631 Products Inhibit Ice Recrystallisation, Attenuate Ice Nucleation, and Reduce Immune Response
632 *Plants (Basel)* **11**, <http://dx.doi.org/10.3390/plants11111475>
- 633 19. Qiu, Y., Hudait, A., and Molinero, V. (2019) How Size and Aggregation of Ice-Binding Proteins
634 Control Their Ice Nucleation Efficiency *J Am Chem Soc* **141**, 7439-7452
635 <http://dx.doi.org/10.1021/jacs.9b01854>
- 636 20. Roeters, S. J., Golbek, T. W., Bregnhøj, M., Drace, T., Alamdari, S., Roseboom, W. *et al.* (2021)
637 Ice-nucleating proteins are activated by low temperatures to control the structure of interfacial
638 water *Nat Commun* **12**, 1183 <http://dx.doi.org/10.1038/s41467-021-21349-3>
- 639 21. Schmid, D., Pridmore, D., Capitani, G., Battistutta, R., Neeser, J.-R., and Jann, A. (1997) Molecular
640 organisation of the ice nucleation protein InaV from *Pseudomonas syringae* *FEBS Letters* **414**,
641 590-594 [http://dx.doi.org/10.1016/s0014-5793\(97\)01079-x](http://dx.doi.org/10.1016/s0014-5793(97)01079-x)
- 642 22. Hartmann, S., Ling, M., Dreyer, L. S. A., Zipori, A., Finster, K., Grawe, S. *et al.* (2022) Structure and
643 Protein-Protein Interactions of Ice Nucleation Proteins Drive Their Activity *Front Microbiol* **13**,
644 872306 <http://dx.doi.org/10.3389/fmicb.2022.872306>
- 645 23. Novikova, I. V., China, S., and Evans, J. E. (2018) Overcoming bottlenecks for in vitro synthesis
646 and initial structural insight of ice nucleating protein InaZ *bioRxiv* 334987
647 <http://dx.doi.org/10.1101/334987>
- 648 24. Li, Q., Yan, Q., Chen, J., He, Y., Wang, J., Zhang, H. *et al.* (2012) Molecular characterization of an
649 ice nucleation protein variant (inaQ) from *Pseudomonas syringae* and the analysis of its
650 transmembrane transport activity in *Escherichia coli* *Int J Biol Sci* **8**, 1097-1108
651 <http://dx.doi.org/10.7150/ijbs.4524>
- 652 25. Li, L., Kang, D. G., and Cha, H. J. (2004) Functional display of foreign protein on surface of
653 *Escherichia coli* using N-terminal domain of ice nucleation protein *Biotechnol Bioeng* **85**, 214-
654 221 <http://dx.doi.org/10.1002/bit.10892>
- 655 26. Nicchi, S., Giuliani, M., Giusti, F., Pancotto, L., Maione, D., Delany, I. *et al.* (2021) Decorating the
656 surface of *Escherichia coli* with bacterial lipoproteins: a comparative analysis of different display
657 systems *Microb Cell Fact* **20**, 33 <http://dx.doi.org/10.1186/s12934-021-01528-z>

- 658 27. Kassmannhuber, J., Rauscher, M., Schoner, L., Witte, A., and Lubitz, W. (2017) Functional display
659 of ice nucleation protein InaZ on the surface of bacterial ghosts *Bioengineered* **8**, 488-500
660 <http://dx.doi.org/10.1080/21655979.2017.1284712>
- 661 28. Kassmannhuber, J., Mauri, S., Rauscher, M., Brait, N., Schoner, L., Witte, A. *et al.* (2020) Freezing
662 from the inside: Ice nucleation in *Escherichia coli* and *Escherichia coli* ghosts by inner membrane
663 bound ice nucleation protein InaZ *Biointerphases* **15**, 031003
664 <http://dx.doi.org/10.1116/1.5142174>
- 665 29. Wick, R. R., Judd, L. M., Gorrie, C. L., and Holt, K. E. (2017) Unicycler: Resolving bacterial genome
666 assemblies from short and long sequencing reads *PLoS Comput Biol* **13**, e1005595
667 <http://dx.doi.org/10.1371/journal.pcbi.1005595>
- 668 30. Chao, H., Sonnichsen, F. D., DeLuca, C. I., Sykes, B. D., and Davies, P. L. (1994) Structure-function
669 relationship in the globular type III antifreeze protein: identification of a cluster of surface
670 residues required for binding to ice *Protein Sci* **3**, 1760-1769
671 <http://dx.doi.org/10.1002/pro.5560031016>
- 672 31. Melnik, T., Povarnitsyna, T., Solonenko, H., and Melnik, B. (2011) Studies of irreversible heat
673 denaturation of green fluorescent protein by differential scanning microcalorimetry
674 *Thermochimica Acta* **512**, 71-75 <http://dx.doi.org/10.1016/j.tca.2010.09.002>
- 675 32. Kajava, A. V., and Steven, A. C. (2006) Beta-rolls, beta-helices, and other beta-solenoid proteins
676 *Adv Protein Chem* **73**, 55-96 [http://dx.doi.org/10.1016/S0065-3233\(06\)73003-0](http://dx.doi.org/10.1016/S0065-3233(06)73003-0)
- 677 33. Lindow, S. E., Arny, D. C., and Upper, C. D. (1982) Bacterial ice nucleation: a factor in frost injury
678 to plants *Plant Physiol* **70**, 1084-1089 <http://dx.doi.org/10.1104/pp.70.4.1084>
- 679 34. Liu, K., Wang, C., Ma, J., Shi, G., Yao, X., Fang, H. *et al.* (2016) Janus effect of antifreeze proteins
680 on ice nucleation *Proc Natl Acad Sci U S A* **113**, 14739-14744
681 <http://dx.doi.org/10.1073/pnas.1614379114>
- 682 35. Cock, P. J., Antao, T., Chang, J. T., Chapman, B. A., Cox, C. J., Dalke, A. *et al.* (2009) Biopython:
683 freely available Python tools for computational molecular biology and bioinformatics
684 *Bioinformatics* **25**, 1422-1423 <http://dx.doi.org/10.1093/bioinformatics/btp163>
- 685 36. Tareen, A., and Kinney, J. B. (2019) Logomaker: Beautiful sequence logos in python *bioRxiv*
686 635029 <http://dx.doi.org/10.1101/635029>
- 687 37. Waterhouse, A. M., Procter, J. B., Martin, D. M., Clamp, M., and Barton, G. J. (2009) Jalview
688 Version 2--a multiple sequence alignment editor and analysis workbench *Bioinformatics* **25**,
689 1189-1191 <http://dx.doi.org/10.1093/bioinformatics/btp033>
- 690 38. Belval, L., Marquette, A., Mestre, P., Piron, M. C., Demangeat, G., Merdinoglu, D. *et al.* (2015) A
691 fast and simple method to eliminate Cpn60 from functional recombinant proteins produced by
692 *E. coli* Arctic Express Protein Expr Purif **109**, 29-34 <http://dx.doi.org/10.1016/j.pep.2015.01.009>
- 693 39. Reicher, N., Segev, L., and Rudich, Y. (2018) The Welzmann Supercooled Droplets Observation
694 on a Microarray (WISDOM) and application for ambient dust Atmospheric Measurement
695 Techniques **11**, 233-248 <http://dx.doi.org/10.5194/amt-11-233-2018>
- 696 40. Braslavsky, I., and Drori, R. (2013) LabVIEW-operated novel nanoliter osmometer for ice binding
697 protein investigations *J Vis Exp* e4189 <http://dx.doi.org/10.3791/4189>

- 698 41. Liu, J., Lin, T., Botkin, D. J., McCrum, E., Winkler, H., and Norris, S. J. (2009) Intact flagellar motor
699 of *Borrelia burgdorferi* revealed by cryo-electron tomography: evidence for stator ring curvature
700 and rotor/C-ring assembly flexion *J Bacteriol* **191**, 5026-5036
701 <http://dx.doi.org/10.1128/JB.00340-09>
- 702 42. Zhao, X., Zhang, K., Boquoi, T., Hu, B., Motaleb, M. A., Miller, K. A. *et al.* (2013) Cryoelectron
703 tomography reveals the sequential assembly of bacterial flagella in *Borrelia burgdorferi* *Proc*
704 *Natl Acad Sci U S A* **110**, 14390-14395 <http://dx.doi.org/10.1073/pnas.1308306110>
- 705 43. Xiang, Y., Surovtsev, I. V., Chang, Y., Govers, S. K., Parry, B. R., Liu, J. *et al.* (2021) Interconnecting
706 solvent quality, transcription, and chromosome folding in *Escherichia coli* *Cell* **184**, 3626-3642
707 e3614 <http://dx.doi.org/10.1016/j.cell.2021.05.037>
- 708 44. Xu, A., and Xu, C. (2021) FastTomo: A SerialEM Script for Collecting Electron Tomography Data
709 *bioRxiv* 2021.2003.2016.435675 <http://dx.doi.org/10.1101/2021.03.16.435675>
- 710 45. Zheng, S. Q., Palovcak, E., Armache, J. P., Verba, K. A., Cheng, Y., and Agard, D. A. (2017)
711 MotionCor2: anisotropic correction of beam-induced motion for improved cryo-electron
712 microscopy *Nat Methods* **14**, 331-332 <http://dx.doi.org/10.1038/nmeth.4193>
- 713 46. Kremer, J. R., Mastronarde, D. N., and McIntosh, J. R. (1996) Computer visualization of three-
714 dimensional image data using IMOD *J Struct Biol* **116**, 71-76
715 <http://dx.doi.org/10.1006/jsbi.1996.0013>
- 716 47. Agulleiro, J. I., and Fernandez, J. J. (2015) Tomo3D 2.0--exploitation of advanced vector
717 extensions (AVX) for 3D reconstruction *J Struct Biol* **189**, 147-152
718 <http://dx.doi.org/10.1016/j.jsb.2014.11.009>
- 719

Supplemental information



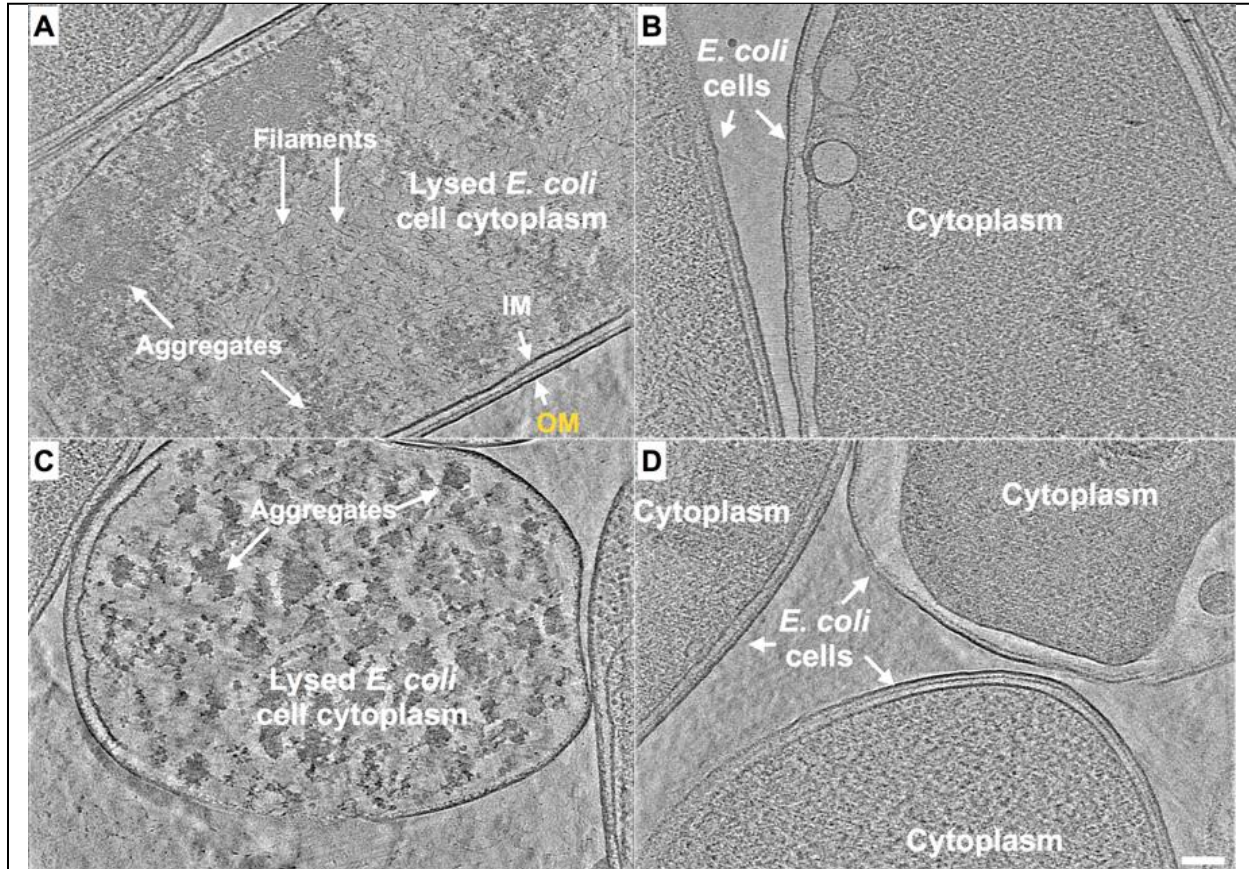


Figure S5. *E. coli* expressing INP mutant lacking R-coils shows no fibre clusters as observed in those cells overexpressing WT INP. **A-D)** Representative snapshots from 3-D cryo-tomograms showing cytoplasmic and extracellular features of various *E. coli* cells overexpressing an INP mutant in which all but the C-terminal R-coil have been replaced by WO-coils. All four images are in the same scale and the scale bar represents 100 nm.